ADVANCED ELECTRONIC MATERIALS
Open Access
www.advelectronicmat.de

Competition between Carrier Injection and Structural Distortions in Electron-Doped Perovskite Nickelate Thin Films

Marios Hadjimichael, Bernat Mundet, Claribel Domínguez, Adrien Waelchli, Gabriele De Luca, Jonathan Spring, Simon Jöhr, Siobhan McKeown Walker, Cinthia Piamonteze, Duncan T. L. Alexander, Jean-Marc Triscone, and Marta Gibert*

The discovery of superconductivity in doped infinite-layer nickelate thin films has brought increased attention to the behavior of the doped perovskite phase. Despite this interest, the majority of existing studies pertain to hole-doped perovskite rare-earth nickelate thin films, while most electron-doping studies have been performed on bulk materials so far. To tackle this imbalance, a detailed study that addresses doping of $NdNiO_3$ thin films using A-site substitution is presented, using Pb as a dopant and taking advantage of its valence-skipping nature. Through a combination of complementary techniques including X-ray diffraction, transport measurements, X-ray absorption spectroscopy, electron energy-loss spectroscopy and scanning transmission electron microscopy, the valence of Pb in the $Nd_{1-x}Pb_xNiO_3$ structure is confirmed to be 4+, and the behavior of the doped thin films is found to be controlled by a competition between carrier injection and structural distortions, which respectively reduce and increase the metal-to-insulator transition temperature. This work provides a systematic study of electron doping in $NdNiO_3$, demonstrating that A-site substitution with Pb is an appropriate method for such doping in perovskite rare-earth nickelate systems.

1. Introduction

Transition metal oxides are characterized by their close proximity to a large range of structural and electronic instabilities, and exhibit complex phase diagrams with a variety of competing phases that can be spanned using chemical substitution. Among them, materials that exhibit metal-to-insulator transitions are especially interesting, as this transition is associated with fluctuations and ordering in the orbital, spin, charge, and lattice degrees of freedom.[1] Due to this proximity to various types of ordering, chemical doping in these materials can lead to many exotic phenomena including colossal magnetoresistance and superconductivity.[2,3]

Rare-earth nickelates ($RNiO_3$, where R is a trivalent rare earth cation) are a canonical example of a material with a bandwidth-controlled metal-to-insulator transition. In these compounds, the

M. Hadjimichael, B. Mundet, C. Domínguez, A. Waelchli, S. McKeown Walker, J.-M. Triscone
Department of Quantum Matter Physics
University of Geneva
24 Quai Ernest-Ansermet, Geneva 1211, Switzerland
E-mail: marios.hadjimichael@unige.ch

B. Mundet, D. T. L. Alexander
Electron Spectrometry and Microscopy Laboratory (LSME)
Institute of Physics (IPHYS)
École Polytechnique Fédérale de Lausanne (EPFL)
Lausanne 1015, Switzerland

The ORCID identification number(s) for the author(s) of this article can be found under https://doi.org/10.1002/aelm.202201182.

DOI: 10.1002/aelm.202201182

G. De Luca
Catalan Institute of Nanoscience and Nanotechnology (ICN2)
Campus UAB, Bellaterra, Barcelona 08193, Spain

J. Spring, S. Jöhr
Physik-Institut
University of Zurich
Winterthurerstrasse 190, Zurich 8057, Switzerland

S. McKeown Walker
Laboratory of Advanced Technology (LTA)
24 Quai Ernest-Ansermet, Geneva 1211, Switzerland

C. Piamonteze
Photon Science Division
Paul Scherrer Institute
Villigen 5232, Switzerland

M. Gibert
Solid State Physics Institute
TU Wien
Wiedner Hauptstr. 8-10/138, Vienna 1040, Austria

size of the rare-earth cation determines the metal-to-insulator transition and the paramagnetic-to-antiferromagnetic transition temperatures.[4–6] As the rare-earth cation size is reduced from La to Lu, the tolerance factor decreases and the RNiO$_3$ structure becomes more distorted, adopting smaller Ni–O–Ni bond angles. This reduces the overlap between Ni 3d and O 2p orbitals (decreasing the bandwidth W) and therefore increases the temperature of the metal-to-insulator transition.[1] Despite their interesting properties, due to the difficulty in making bulk materials, the study of rare-earth nickelates and the full exploitation of their potential were initially limited. The possibility of depositing these systems as high-quality epitaxial thin films renewed attention on the nickelates, with studies on the effect of strain,[7–12] heterostructuring,[13–19] field effect,[9,20,21] thickness,[22–24] and optical excitations.[25–27]

The rare-earth nickelate family has recently attracted further interest due to the discovery of superconductivity in infinite-layer NdNiO$_2$ thin films hole doped with Sr,[28] a phase achieved by topotactic reduction of the perovskite Nd$_{1-x}$Sr$_x$NiO$_3$ phase. After this discovery, films with a range of rare earth cations (R = La, Pr, and Nd) and different dopants (Sr and Ca) were found to exhibit superconductivity,[29–33] including the functionally-doped Nd$_6$Ni$_5$O$_{12}$ phase.[34] So far, superconductivity has only been observed in infinite-layer nickelate thin films, but not in bulk single crystals or powders.[35,36] The study of doped rare-earth nickelates in thin film form is therefore critical to provide deeper understanding into the behavior of both the perovskite and the infinite-layer phases.

The RNiO$_3$ compounds are negative charge-transfer insulators and their behavior is therefore extremely sensitive to electronic doping.[1] This doping can be achieved using an electric field,[9,21,22,37] by oxygen off-stoichiometry control[38–43] or by chemical substitution of the rare earth cation (with a nominal valence of 3+) with another cation of a different valence.[44–47] Both electron and hole doping have been shown to reduce the metal-to-insulator transition temperature (T_{MI}) in bulk powders of NdNiO$_3$ when doped with Ca^{2+}, Sr^{2+}, Th^{4+}, and Ce^{4+}, at different rates depending on the dopant used.[44–47] In these doped compounds, the T_{MI} is affected both by charge carrier injection, and by the change in the Ni–O–Ni bond angles that arises due to the difference in the size of Nd compared to the divalent or tetravalent dopants.[47] Carrier injection reduces the T_{MI} for both electron and hole doping, but the effect of A-cation size on the T_{MI} is opposite depending on whether the dopant is larger or smaller than Nd. In the case of doping with Ca^{2+} and Sr^{2+}, both ions have a larger ionic radius than Nd^{3+},[48] therefore reducing the magnitude of the structural distortions and increasing the Ni–O–Ni bond angle with doping, thus making the octahedral rotations less pronounced. The increase in the Ni–O–Ni bond angle cooperates with the carrier injection and reduces the T_{MI} even further. Conversely, the ionic radii of Th^{4+} and Ce^{4+} are smaller than Nd^{3+}, increasing the distortions in the structure and reducing the Ni–O–Ni bond angle with doping, making the octahedral rotations more pronounced. This reduction in the Ni–O–Ni bond angle increases T_{MI} and therefore competes with the carrier injection, making the suppression of T_{MI} as a function of doping less dramatic.

Despite the comprehensive results on both hole- and electron-doped NdNiO$_3$ bulk samples,[44–47] as well as the renewed interest in chemically-substituted nickelates after the discovery of superconductivity in Nd$_{1-x}$Sr$_x$NiO$_2$,[28] systematic studies of doped perovskite rare-earth nickelate films are still lacking, with most works focusing on hole-doped films with Ca or Sr.[29–31,49,50] More importantly, the effects of electron doping through chemical substitution in RNiO$_3$ thin films have not been investigated yet, and are crucial for advancing our understanding of these materials and for the development of electron-doped infinite-layer nickelate superconductors.

In this work, we electron dope NdNiO$_3$ thin films using A-site substitution. Given the radioactive nature of thorium and the possibility of adopting a valence of 3+ and 4+ in cerium, our approach instead consists of doping NdNiO$_3$ with Pb. To do so, we use off-axis radiofrequency magnetron sputtering to fabricate Nd$_{1-x}$Pb$_x$NiO$_3$ thin films (x = 0–0.08) of high structural quality on NdGaO$_3$ substrates. Resistivity measurements as a function of temperature show that the T_{MI} decreases with increasing Pb content. However, despite doping levels up to x = 0.08, the metal-to-insulator transition persists and the films do not become fully metallic at low temperatures. Using a combination of X-ray absorption spectroscopy (XAS) and electron energy-loss spectroscopy (EELS), we show that the films are electron-doped, with a nominal Ni valence shifting from 3+ toward 2+ with increasing Pb content. Finally, we use aberration-corrected scanning transmission electron microscopy (STEM) to map the atomic positions of the A (Nd/Pb) and B (Ni) sites, and extract the magnitude of the structural distortions in the Nd$_{1-x}$Pb$_x$NiO$_3$ thin films. We find that when we introduce Pb into the structure the distortions become larger, signifying a smaller Ni–O–Ni bond angle due to more pronounced octahedral rotations. This allows us to conclude that Pb has a smaller ionic radius compared to Nd, consistent with Pb in a 4+ valence.

2. Results

2.1. Deposition and Structure of Nd$_{1-x}$Pb$_x$NiO$_3$ Thin Films

Bulk NdNiO$_3$ is orthorhombic, with a pseudocubic unit cell with lattice parameter of 3.808 Å and an average Ni–O–Ni bond angle of ≈157°.[51] It displays a metal-to-insulator transition at 200 K with a simultaneous appearance of antiferromagnetic order.[52–54] Bulk PbNiO$_3$ is hexagonal and its structure can be expressed using a rhombohedral subcell, with lattice parameter of 3.886 Å and α_r = 87.26°.[55] It is semiconducting, with an antiferromagnetic transition temperature of ≈205 K.[55] The average Ni–O–Ni bond angle in PbNiO$_3$ is ≈137°, and in this system Pb is in a 4+ valence, making it the first observed perovskite structure with Pb in a fully tetravalent state.[56]

The solid solution Nd$_{1-x}$Pb$_x$NiO$_3$ thin films were deposited by sequential sub-monolayer deposition from two different sputtering targets, NdNiO$_3$ and Pb$_{1.1}$NiO$_3$, as described in Experimental Section. After a preliminary calibration of the rates of the two constituent materials, the precise Pb content of each Nd$_{1-x}$Pb$_x$NiO$_3$ film was determined after deposition using energy-dispersive X-ray spectroscopy (EDX) performed on the cross-section of each film (see Experimental Section). To achieve the growth of films with high homogeneity, a capping

ADVANCED ELECTRONIC MATERIALS
Open Access
www.advelectronicmat.de

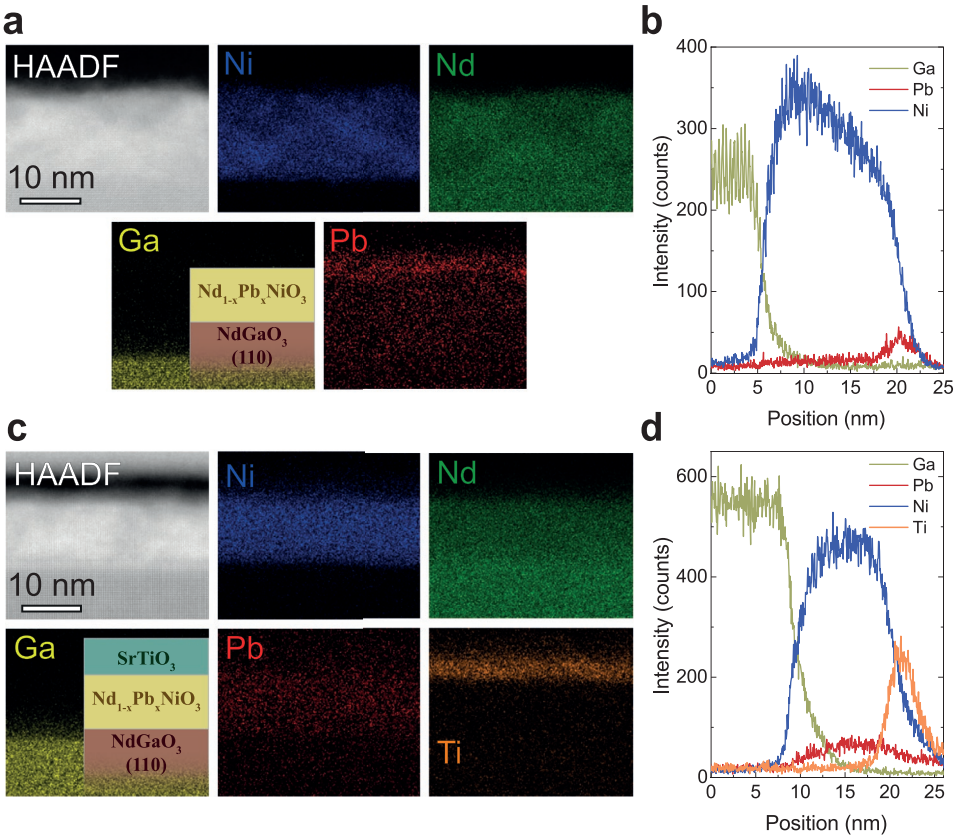

Figure 1. EDX measurements of two $Nd_{1-x}Pb_xNiO_3$ thin films deposited under identical growth conditions, showing the importance of the $SrTiO_3$ capping layer. a) EDX analysis of a $Nd_{1-x}Pb_xNiO_3$ film with estimated $x = 0.07$ (from individual material growth rates), without any capping layer. The analysis shows that most of the Pb has migrated to the surface. A Pb/(Pb+Nd) atomic percentage of 1–2% is found in the bulk of the film, whereas 20% is found on the surface. b) EDX profiles of the film without any capping layer showing the large concentration of Pb on the surface. c) EDX analysis of a $Nd_{1-x}Pb_xNiO_3$ film with $x = 0.07$, deposited under identical growth conditions and capped with 5 unit cells of $SrTiO_3$. The images show a uniform Pb distribution across the thickness of the film, with a Pb/(Pb+Nd) atomic percentage of 7%. d) EDX profiles of the film capped with 5 unit cells of $SrTiO_3$, where the uniform Pb distribution is clear. The Nd profiles in (b) and (d) are not shown for clarity, as their behavior is identical for both films.

layer has to be deposited immediately after the deposition of the Pb-doped $NdNiO_3$. **Figure 1**a is an EDX map of a $Nd_{1-x}Pb_xNiO_3$ film deposited on a (110)-oriented $NdGaO_3$ substrate with a free surface. We find that this film (as well as other $Nd_{1-x}Pb_xNiO_3$ films with free surfaces) shows Pb migration to the surface, with a Pb/(Pb+Nd) atomic percentage of ≈20% concentrated in the surface of the sample while a much smaller percentage (≈1–2%) remains in the bulk of the film. The migration of Pb to the surface of the film is confirmed in Figure 1b, a plot of the EDX line profiles for Ga (present only in the substrate), Pb and Ni for this uncapped $Nd_{1-x}Pb_xNiO_3$ film. The Pb profile peaks close to the surface of the deposited $Nd_{1-x}Pb_xNiO_3$ layer, due to the large concentration of Pb on the surface as compared to the rest of the film.

The deposition of the $SrTiO_3$ capping layer (in this case, 5 unit cells of $SrTiO_3$) stops the migration of Pb to the surface, rendering the distribution of Pb across the film uniform (see Experimental Section for growth conditions of $SrTiO_3$). An EDX map of a capped film (with $Nd_{1-x}Pb_xNiO_3$ deposited in identical conditions as the uncapped case) is shown in Figure 1c, with a uniform Pb concentration of 7% in this case. A plot of the EDX profiles for Ga, Pb, Ni, and Ti for the capped $Nd_{1-x}Pb_xNiO_3$ film shown in Figure 1d clearly indicates that the Pb profile is constant throughout the thickness of the film.

The exact origin of the Pb migration to the surface and the effect of capping is unclear, but it is most likely due to the highly volatile nature of Pb and its interaction with oxygen species in the chamber during growth.[57,58] Consistent with this assumption, in some uncapped films in which we aimed for a large concentration of Pb we have observed weak peaks in the X-ray diffraction scans that could be consistent with PbO or Pb_3O_4. Based on these results, all $Nd_{1-x}Pb_xNiO_3$ films that have been studied in this work have been capped with 5 unit cells of $SrTiO_3$ to maintain a uniform Pb content and a high structural quality.

Figure 2a is a plot of large-range specular θ–2θ X-ray diffraction scans for a series of $Nd_{1-x}Pb_xNiO_3$ thin films ($x = 0$ up to $x = 0.08$) deposited on (110)-oriented $NdGaO_3$ substrates and capped with 5 unit cells of $SrTiO_3$. The scans display intense Bragg peaks associated with the perovskite unit cell of the film, and no parasitic phases. As shown in Figure 2b, the θ–2θ scans are characterized by sharp finite-size oscillations, indicating a well-defined thickness and high structural quality. Additionally, the quality of the $Nd_{1-x}Pb_xNiO_3$ thin films is confirmed using

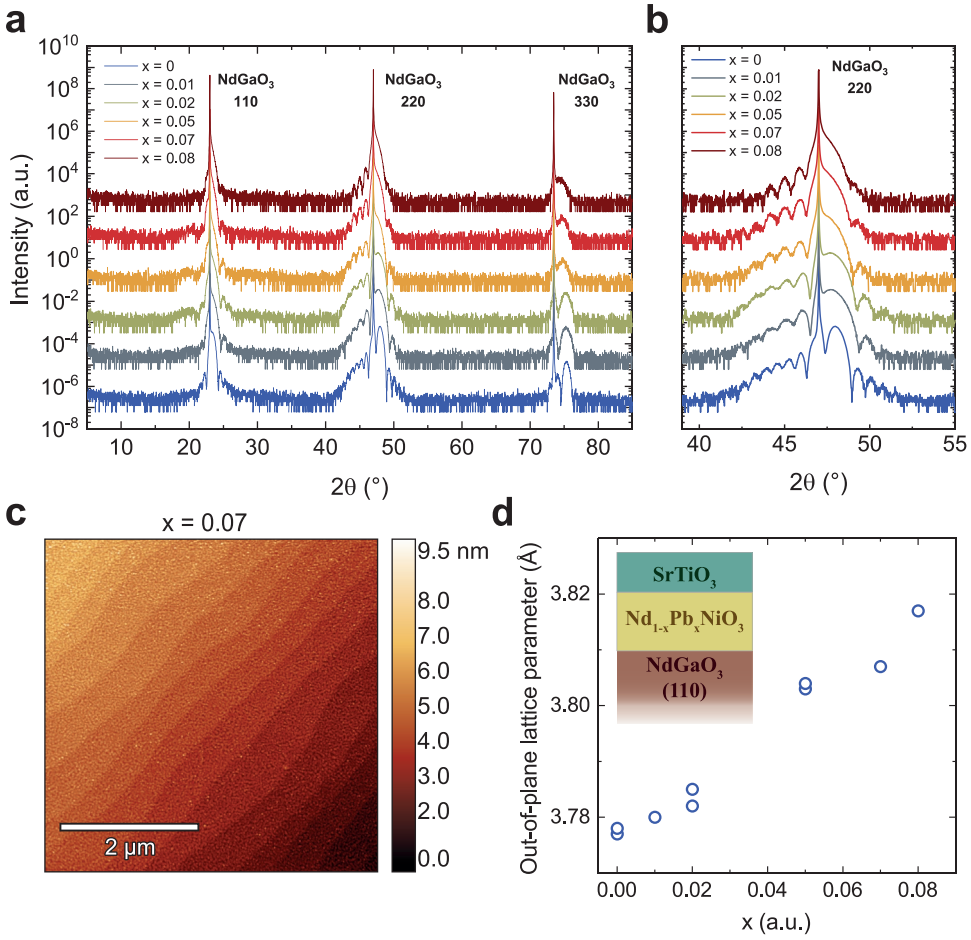

Figure 2. Structural characterization of $Nd_{1-x}Pb_xNiO_3$ films deposited on $NdGaO_3$, capped with 5 unit cells of $SrTiO_3$. a) Large-range θ–2θ scans of a series of $Nd_{1-x}Pb_xNiO_3$ thin films, showing finite-size oscillations and no parasitic phases. The films are ≈22–30 unit cells (8–10 nm) thick and are capped with 5 unit cells of $SrTiO_3$. b) Short-range θ–2θ scans around the orthorhombic 220 peak of $NdGaO_3$. c) Atomic force microscopy image of a film with $x = 0.07$, characterized by unit-cell-high steps and a flat surface morphology. d) Evolution of the out-of-plane lattice parameter of the $Nd_{1-x}Pb_xNiO_3$ thin films as a function of Pb content, x.

atomic force microscopy (AFM). Figure 2c is an AFM scan for a sample with $x = 0.07$, showing that the film has a flat surface morphology with a roughness smaller than one unit cell, as well as unit-cell-high steps. Similarly, all studied compositions exhibit atomically flat surfaces, as seen in Figure S1, Supporting Information. We note that we were unable to deposit any high-quality $Nd_{1-x}Pb_xNiO_3$ films with $x > 0.08$, since a drastic degradation of their structural quality occurs for such Pb concentrations. For this reason, only films with Pb content up to 8% are studied in this work.

The lattice parameters and the thickness of the $Nd_{1-x}Pb_xNiO_3$ and $SrTiO_3$ layers can be extracted from the profile of the 002 peak by simulating the θ–2θ scans using a kinematic scattering model developed in ref. [59], by simulating the scattered intensity from a bilayer of $NdNiO_3$ and $SrTiO_3$ on top of a $NdGaO_3$ substrate. Figure S2, Supporting Information shows the simulated diffraction patterns and their comparison with the experimental measurements, evidencing excellent agreement. No significant differences are found in the simulated diffractograms if a $Nd_{1-x}Pb_xNiO_3$ solid solution is modeled instead of $NdNiO_3$, most likely due to the small Pb content.

Figure 2d is a plot of the extracted out-of-plane lattice parameter of $Nd_{1-x}Pb_xNiO_3$ as a function of Pb content, x. The out-of-plane lattice parameter increases as the Pb content increases, indicating an expansion in the volume of the unit cell, as observed in electron-doped polycrystalline samples[44–47] as well as bulk samples and thin films doped with F, Li, or oxygen vacancies.[38,60–63] We note that this change in lattice parameter is not associated with strain relaxation, since the $Nd_{1-x}Pb_xNiO_3$ films remain strained to the $NdGaO_3$ substrate, as seen in the reciprocal space map around the $\bar{1}03$ pseudocubic $NdGaO_3$ peak for a sample with $x = 0.05$ (Figure S3, Supporting Information).

2.2. Transport Properties of $Nd_{1-x}Pb_xNiO_3$ Thin Films

To understand the effect of Pb-doping on the electronic properties of the $Nd_{1-x}Pb_xNiO_3$ thin films we measure their resistivity as a function of temperature. **Figure 3**a is a plot of the resistivity versus temperature for a series of $Nd_{1-x}Pb_xNiO_3$ thin films with x ranging from 0 to 0.08, with the cooling and heating branch

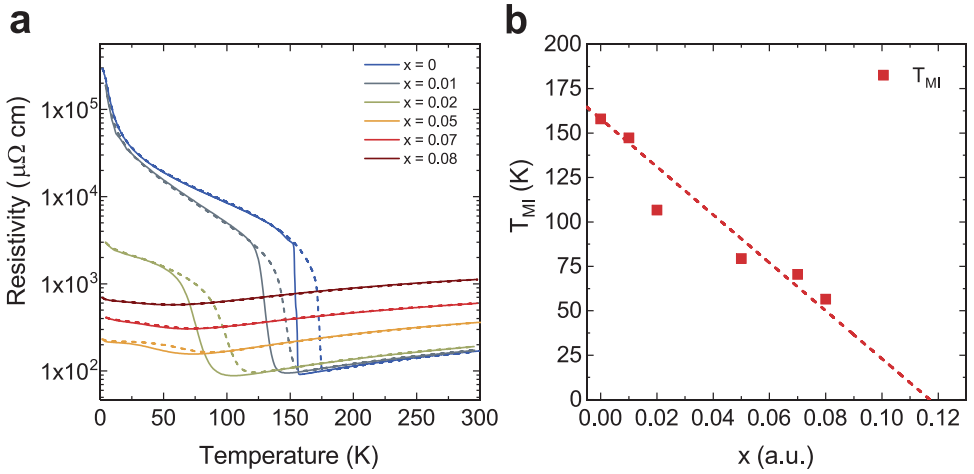

Figure 3. Transport properties of $Nd_{1-x}Pb_xNiO_3$ films deposited on $NdGaO_3$. a) Resistivity (in logarithmic scale) as a function of temperature for a series of $Nd_{1-x}Pb_xNiO_3$ thin films, showing the upturn in temperature due to the metal-to-insulator transition. The solid and dashed lines indicate resistivity values measured upon cooling and heating respectively. b) Metal-to-insulator transition temperatures (T_{MI}) as a function of doping x for the studied films. The dashed line is a linear fit to the T_{MI} data points ($T_{MI} = mx + c$), with gradient m = (–1350 ± 110) K and intercept c = 158 K, fixed to the T_{MI} of the undoped film.

of the resistivity indicated by solid and dashed lines respectively. All studied films show a characteristic jump due to the metal-to-insulator transition.[64] This can be seen more clearly in a smaller-scale plot of the resistivity in Figure S4, Supporting Information, where the upturn due to the metal-to-insulator transition still occurs even for the highest Pb concentrations. Additionally, as clearly seen in the behavior of the films with the lowest Pb concentrations, the behavior of the resistivity is hysteretic due to the first-order nature of the transition in $NdNiO_3$.[4,65] The hysteretic behavior of the resistivity persists as the films are doped with Pb, but the width of the hysteresis is reduced with doping. At the moment, it is unclear whether this effect could be attributed to behavior that is intrinsic to the material, or associated with a change in sample quality with doping,[54] and to clarify the reason for this behavior further investigation is required. Finally, our measurements show that as the Pb concentration increases, two dominant effects are observed in the transport properties of the films: i) the T_{MI} decreases from ≈150 K for pure $NdNiO_3$ (x = 0) to 57 K for $Nd_{0.92}Pb_{0.08}NiO_3$ (x = 0.08), and ii) the room-temperature resistivity increases.

The effect of Pb-doping on the T_{MI} is summarized in Figure 3b, a plot of the temperature at which the onset of the metal-to-insulator transition occurs for each sample during cooling, defined as the minimum of the resistivity on the cooldown branch. The plot shows that despite Pb-doping levels up to 8%, the metal-to-insulator transition persists, and the samples do not become completely metallic up to these doping levels. This is in contrast to hole-doped (A-site substitution using Ca and Sr) $NdNiO_3$ thin films and bulk samples, where a complete suppression of the metal-to-insulator transition occurs at around x = 0.05–0.07.[29,44–47,50]

In ref. [47], García-Muñoz and co-workers were able to isolate the effect of the carrier injection on the T_{MI} of $NdNiO_3$ from the change in the cation size with doping using the following equation:

$$\left(\frac{dT_{MI}(x,R_0(x))}{dx}\right)=\left(\frac{\partial T_{MI}(x,R_0(x))}{\partial x}\right)_{R_0=R_0[Nd]}+\left(\frac{\partial T_{MI}(x,R_0(x))}{\partial R_0}\right)_{x=0}\frac{dR_0(x)}{dx} \quad (1)$$

Here, dT_{MI}/dx is the observed dependence of T_{MI} on doping (carrier injection and change in A-cation size), $\partial T_{MI}/\partial x$ is the dependence of T_{MI} on carrier injection only, $\partial T_{MI}/\partial R_0$ is the dependence of T_{MI} on the A-cation size and dR_0/dx is the change in the ionic radius of the A-cation with respect to Nd as a function of doping. The authors have found that the measured suppression rate of the T_{MI}, dT_{MI}/dx, is drastically different for Sr (–4190 K), Ca (–3180 K), Th (–1029 K), and Ce (–220 K). Additionally, they found that the extracted suppression rate of the T_{MI} when cation size effects are removed is $(\partial T_{MI}/\partial x)_h \approx -3200$ K for holes and $(\partial T_{MI}/\partial x)_e \approx -1200$ K for electrons, reflecting the large electron–hole asymmetry in this system.

We have fitted the data of Figure 3b using a straight line, fixing the intercept at $x = 0$ to be equal to 158 K, the T_{MI} of the undoped film. We find that the observed gradient, dT_{MI}/dx, is equal to (–1350 ± 110) K, comparable to the values measured by García-Muñoz and co-workers for electron-doped bulk samples.[47] Additionally, the linear fit of Figure 3b shows that the T_{MI} would be completely suppressed at a Pb content of 12%, much higher than the equivalent value for hole-doped bulk samples and thin films. As mentioned previously, such a high Pb content could not be reached due to a drastic degradation in sample quality for $x > 0.08$.

For our $Nd_{1-x}Pb_xNiO_3$ thin films, expressing the change of the T_{MI} as a function of known quantities similarly to Equation (1) is more complicated than the case of bulk samples, since the magnitude of the epitaxial strain changes as we dope with Pb. By increasing the Pb content we move from the smaller pseudocubic unit cell of $NdNiO_3$[51] toward the larger pseudocubic unit cell of $PbNiO_3$,[55] therefore making the strain less tensile and so reducing the T_{MI}.[9,10,66] Nevertheless, to confirm that the observed reduction of the T_{MI} is

primarily due to a true electronic doping effect and is not just an effect of the change of strain with Pb doping, we calculate the expected change of the T_{MI} as a function of the latter. Assuming that Vegard's law is valid in the $Nd_{1-x}Pb_xNiO_3$ system, we expect the pseudocubic in-plane lattice parameter of bulk $Nd_{1-x}Pb_xNiO_3$ to have the following doping dependence: $a = 3.808 + (3.886 - 3.808)x$. When bulk $Nd_{1-x}Pb_xNiO_3$ is strained on $NdGaO_3$, the in-plane percentage strain is equal to $\varepsilon = (3.86 - a)/a \times 100$. The dependence of the in-plane percentage strain on doping, x, can then be calculated for small values of x: $\partial\varepsilon/\partial x = -2.07$.

To calculate the dependence of the T_{MI} on the change of strain, we deposited undoped $NdNiO_3$ on $LaAlO_3$ (in-plane lattice parameter equal to 3.79 Å, $\varepsilon = -0.47\%$), $NdGaO_3$ (in-plane lattice parameter equal to 3.86 Å, $\varepsilon = 1.37\%$) and $SrTiO_3$ (in-plane lattice parameter equal to 3.905 Å, $\varepsilon = 2.55\%$). The T_{MI} of each film, determined by measuring their resistivity versus temperature, is 90, 152, and 200 K respectively. This allows us to calculate the strain-dependence of the T_{MI}, finding $\partial T_{MI}/\partial\varepsilon = -36$ K.

The expected dependence of the T_{MI} on the change of the percentage of strain induced by doping (without accounting for any electronic effects) can therefore be calculated as follows

$$\frac{dT_{MI}(x,\varepsilon)}{dx} = \left(\frac{\partial T_{MI}}{\partial\varepsilon}\right)\frac{\partial\varepsilon}{\partial x} = -74.5\ \text{K}. \quad (2)$$

This rate is much smaller than the experimentally observed gradient, $dT_{MI}/dx = -1350$ K, showing that the reduction of the T_{MI} cannot be explained only by a change in strain and that the electronic doping also has to be taken into account.

The second observed effect in the plot of the resistivity as a function of temperature is the increase of the room-temperature resistivity with increasing Pb content. This likely occurs due to disorder introduced by the A-site substitution, as observed in doped bulk samples[44–47] and thin films.[29,49,50] Additionally, defects like oxygen vacancies can also contribute to the increase of the room temperature resistivity,[38,42,43] and these defects can also appear in our $Nd_{1-x}Pb_xNiO_3$ thin films. To decouple the effect of Pb-doping through A-site substitution and oxygen vacancies that could develop during growth, we have annealed a $Nd_{0.98}Pb_{0.02}NiO_3$ ($x = 0.02$) and a $Nd_{0.93}Pb_{0.07}NiO_3$ ($x = 0.07$) thin film in flowing oxygen for various steps as described in Figure S5, Supporting Information. The θ–2θ scans for both films show a shift of the Bragg peak to higher angles, and therefore a decrease in the out-of-plane lattice parameter with annealing (a percentage decrease of 0.05% and 0.4% for the $x = 0.02$ and the $x = 0.07$ films respectively). This reduction in the volume of the unit cell indicates that oxygen vacancies in the as-grown film are being filled with each annealing step. Nevertheless, the resistivity of the films as a function of temperature indicates that even though the room-temperature resistivity decreases with each annealing step, the T_{MI} does not change significantly, consistent with the effect of oxygen vacancies studied in bulk $NdNiO_3$ samples[38] and thin films.[42,43] This allows us to conclude that the observed decrease of the T_{MI} is predominantly due to doping with Pb and not the effect of defects like oxygen vacancies.

2.3. Spectroscopic Evidence for Electron Doping in $Nd_{1-x}Pb_xNiO_3$

To shed light on the effect of Pb doping on the valence of Ni, we use a combination of XAS and STEM-EELS. **Figure 4**a shows X-ray absorption spectra around the Ni $L_{2,3}$ edges for the series of capped $Nd_{1-x}Pb_xNiO_3$ films with x ranging from 0 to 0.07. The top spectrum is a reference spectrum for Ni^{2+}, measured using a NiO powder. In this spectrum, the main peaks at the L_2 and L_3 edges correspond to transitions from Ni $2p_{1/2}$ to Ni 3d and from Ni $2p_{3/2}$ to Ni 3d orbitals, and occur at ≈868 and 851 eV respectively. For Ni in a nominal 2+ valence, the predominant transitions are labeled as $2p^63d^8 \rightarrow 2p^53d^9$.[67] The bottom spectrum in Figure 4a is a reference spectrum from a pure $NdNiO_3$ film with a free surface, deposited on $NdGaO_3$. In this system, the nominal Ni valence is 3+, with features in the spectra predominantly due to a mixture of $2p^63d^7 \rightarrow 2p^53d^8$ and $2p^63d^8\underline{L} \rightarrow 2p^53d^9\underline{L}$ transitions, where $\underline{L}$ denotes an oxygen 2p hole.[68–71] This configuration is associated with clear spectroscopic features in the Ni $L_{2,3}$ edges, which can be observed clearly in this reference Ni^{3+} spectrum.[70]

The spectra for the $SrTiO_3$-capped $Nd_{1-x}Pb_xNiO_3$ thin films as a function of doping in Figure 4a demonstrate that, starting from a nominally Ni^{3+} valence for $x = 0$, a redistribution of the Ni $L_{2,3}$ intensity and a shift of the center of mass of the L_2 and L_3 peaks toward lower energies occurs as Pb is added to the films. This shift toward lower energies is associated with the appearance of a Ni^{2+} component, as demonstrated in the reference spectrum of NiO. The Ni^{2+} features become more intense with increasing Pb content (x), signifying a gradual increase in the Ni^{2+} percentage (as seen more clearly in Figure 4b, where the spectra around the Ni L_3 edge are plotted). The increase in the Ni^{2+} percentage with increasing Pb content confirms electron doping in the system.[63]

Figure 4c is a plot of the electron energy-loss spectra around the Ni $L_{2,3}$ edges for an uncapped $NdNiO_3$ ($x = 0$, blue) and a $Nd_{0.93}Pb_{0.07}NiO_3$ film capped with $SrTiO_3$ ($x = 0.07$, red). The spectra were acquired from the middle of each film using exactly the same acquisition conditions for both samples, by preparing both TEM specimens on the same Cu grid (see Figure S6, Supporting Information and Experimental Section). The substitution of Pb for Nd in the $NdNiO_3$ structure leads to a change in the Ni $L_{2,3}$ spectral shapes that is similar to the change observed in the X-ray absorption spectra of Figure 4a. In contrast, the Nd $M_{4,5}$ spectral shapes do not change with Pb doping, as shown in Figure 4d, indicating that there is no change in the valence of Nd. The spectroscopy studies summarized in Figure 4a–c therefore demonstrate that there is a clear shift from a nominal Ni 3+ valence toward 2+ as the samples are doped with Pb, providing clear evidence for a 4+ Pb valence in this system.

Having confirmed this change from Ni^{3+} valence toward a Ni^{2+} character, we now turn to verifying the homogeneity of the Ni valence in the Pb-doped film. Figure 4e is a plot of the EELS measurements around the Ni $L_{2,3}$ edges for the $x = 0.07$ film, at different positions through the thickness of the film as defined in Figure S6, Supporting Information. We find that the peaks do not change in shape or position as we move from the bottom interface with $NdGaO_3$ to the middle of the film

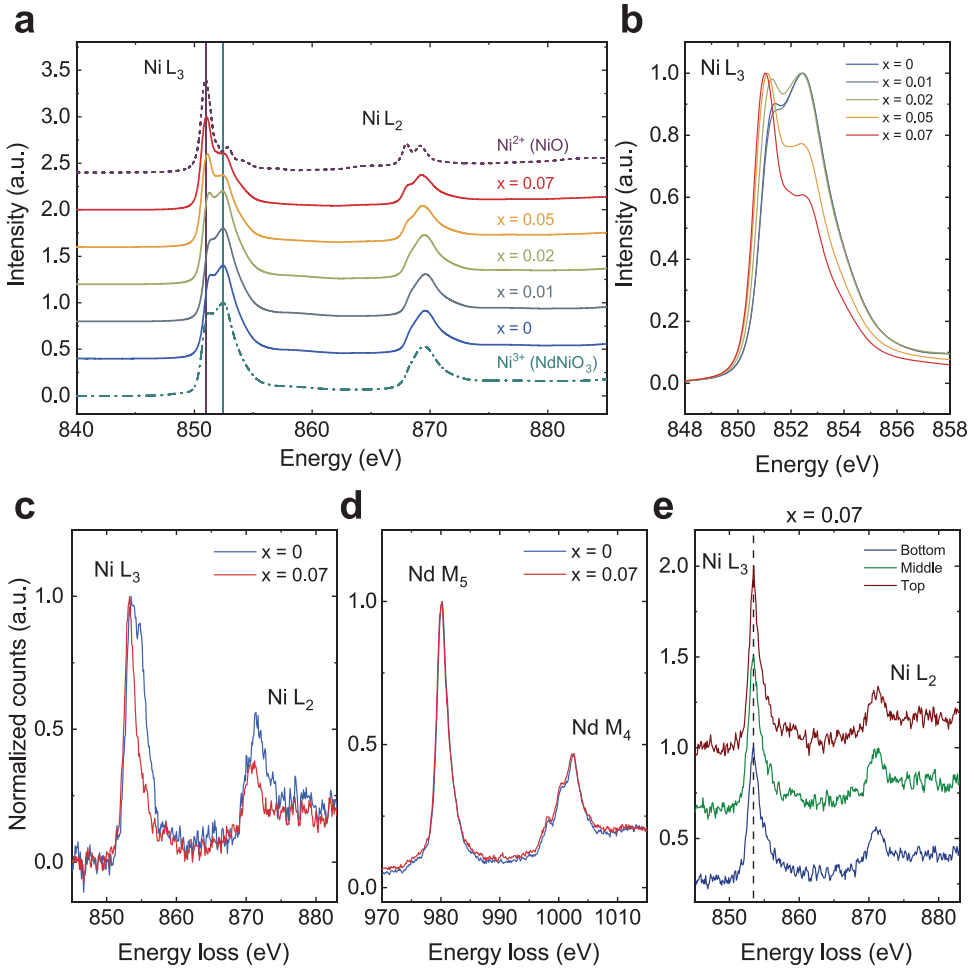

Figure 4. Spectroscopic evidence of increasing content of Ni^{2+} with Pb doping. a) X-ray absorption spectra around the Ni $L_{2,3}$ edges for a series of $Nd_{1-x}Pb_xNiO_3$ thin films as a function of Pb concentration (shifted vertically for clarity). The films are deposited on $NdGaO_3$ and are capped with 5 unit cells of $SrTiO_3$. The bottom spectrum is a reference spectrum for Ni^{3+} (uncapped $NdNiO_3$ thin film deposited on $NdGaO_3$), with the vertical line at 852.4 eV indicating the position of the main Ni^{3+} peak at the L_3 edge. The top spectrum is a reference spectrum for Ni^{2+} (NiO powder), with the vertical line at 851.0 eV indicating the position of the main Ni^{2+} L_3 peak. With Pb doping, the spectra demonstrate the appearance of an additional Ni^{2+} character and its gradual increase in intensity as the Pb content is increased from $x = 0$ to $x = 0.07$. b) Short-range spectra around the Ni L_3 edge showing the details of the increase in the Ni^{2+} percentage. c) Electron energy-loss spectra around the Ni $L_{2,3}$ edges for a $NdNiO_3$ ($x = 0$, blue) and a $Nd_{0.93}Pb_{0.07}NiO_3$ film ($x = 0.07$, red) show a similar trend as the XAS measurements as function of Pb doping. d) EELS measurements around the Nd $M_{4,5}$ edges, showing no changes with Pb doping. e) Spatially resolved electron energy-loss spectra around the Ni $L_{2,3}$ edges for the $x = 0.07$ film, shifted vertically for clarity. From top to bottom: top interface with $SrTiO_3$, middle part of film, and bottom interface with $NdGaO_3$. The position of each region labeled in (e) is indicated in Figure S6, Supporting Information. The vertical dashed lines mark the approximate position of the peak. The plots in (b)–(e) are normalized by the maximum intensity of each spectrum for easier comparison.

and toward the top interface with the $SrTiO_3$ capping layer (see Figure S6c,d, Supporting Information for an overlay of the Ni $L_{2,3}$ and Nd $M_{4,5}$ spectra). This indicates that the Ni valence is homogeneous over the whole film, due to its uniform stoichiometry, consistent with the cross-sectional EDX data in Figure 1c.

These complementary spectroscopy techniques indicate that there is a clear shift from a nominal Ni 3+ valence toward 2+ as the samples are doped with Pb. Similar valence shifts have been observed in perovskite nickelate thin films with strain- or annealing-induced oxygen vacancies,[72,73] as well as hydrogen- and lithium-doped films.[39,62,74] Therefore we would like to discuss next the fundamental differences between electron-doping due to A-site chemical substitution versus doping due to oxygen vacancies or hydrogen/lithium incorporation.

First of all, in the case of doping with hydrogen or lithium, the H^+ and Li^+ ions are incorporated as interstitials, binding with oxygen from existing NiO_6 octahedra without replacing existing atoms in the structure.[62,74] Additionally, oxygen vacancies modify the NiO_6 octahedral configuration and alter the crystal-field splitting accordingly.[63] In contrast, A-site substitution in the $RNiO_3$ structure does not alter the coordination environment of Ni, and for this reason, a direct comparison of the structural effects only taking into account the ionic radius of the various dopants cannot be made.

Second, the appearance of Ni^{2+} due to doping with hydrogen,[39,74] lithium,[62] or strain- or annealing-induced oxygen vacancies[72,73] would lead to localization.[63] As discussed in the previous section, this type of doping should not change the T_{MI}, but will increase the resistivity of the film in the metallic phase, and above a specific threshold of dopants the films will become insulating. On the other hand, the appearance of Ni^{2+} due to doping using A-site substitution will reduce the T_{MI}, as observed in Figure 3. This is expected for any type of Mott insulator when we move away from half-filling by introducing holes or electrons into the system,[1] and is consistent with the behavior observed in the studied $Nd_{1-x}Pb_xNiO_3$ films.

2.4. Scanning Transmission Electron Microscopy Studies of the Structural Distortions

This electron doping through A-site substitution is expected to decrease the T_{MI} at a rate slower than hole-doped films.[47] Additionally, the suppression rate of the T_{MI} will also depend on the change of the Ni–O–Ni bond angle of $Nd_{1-x}Pb_xNiO_3$ as a function of doping, which in turn depends on the valence of Pb. The ionic radius of Pb^{2+} is larger than Nd^{3+},[48] and would therefore lead to a shift of the Ni–O–Ni bond angle toward 180° with increasing Pb content x, making the octahedral rotations in the $Nd_{1-x}Pb_xNiO_3$ structure less pronounced. In contrast, the ionic radius of Pb^{4+} is smaller than Nd^{3+},[48] and its incorporation in the structure would cause the films to adopt smaller Ni–O–Ni bond angles due to stronger octahedral rotations.[55]

To qualitatively estimate the change in the Ni–O–Ni bond angles between samples with different Pb content and to conclusively determine the valence of Pb in the $Nd_{1-x}Pb_xNiO_3$ structure, we use STEM. **Figure 5**a shows a high-resolution high-angle annular dark-field (HAADF) image of a $Nd_{0.93}Pb_{0.07}NiO_3$ (x = 0.07) thin film deposited on $NdGaO_3$, capped with 5 unit cells of $SrTiO_3$, showing sharp and coherent interfaces and no visible dislocations or other lattice defects. Since the intensity in the HAADF image is roughly proportional to the square of the atomic number of each atomic column, the brightest atoms in the image are the A-site cations Nd/Pb, and the second brightest atoms are Ni. In this measurement configuration, the oxygen atoms are not visible.

We can extract the positions of the A-site cations as described in Methods, and use them as a proxy for the degree of distortion in the $RNiO_3$ structure compared to the ideal cubic perovskite lattice. When imaging in the plane defined by the $[001]_o$ and $[110]_o$ directions, we observe a projection of the antipolar displacements

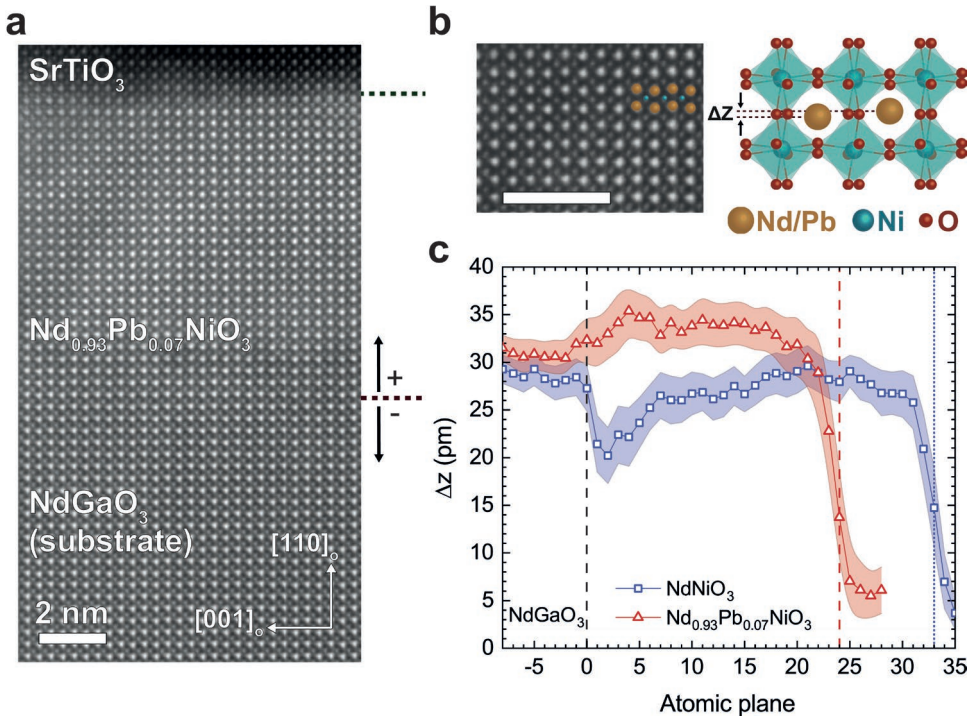

Figure 5. Visualization of increased structural distortions with scanning transmission electron microscopy (STEM). a) High-resolution HAADF image of a $SrTiO_3/Nd_{0.93}Pb_{0.07}NiO_3/NdGaO_3$ (x = 0.07) heterostructure showing sharp and coherent interfaces (indicated by the horizontal dashed lines) and no visible dislocations or other lattice defects. The orthorhombic directions are defined by the arrows. b) Left: magnified region of the $Nd_{0.93}Pb_{0.07}NiO_3$ thin film showing the projection of the antipolar cation displacements, consistent with the schematic of the $NdNiO_3$ crystal structure sketched on the right. The magnitude of the displacements is defined as ΔZ and is proportional to the degree of structural distortion in $RNiO_3$ (a larger ΔZ corresponds to a smaller Ni–O–Ni bond angle). Scale bar: 2 nm. c) Plot of ΔZ as a function of atomic plane position for a pure $NdNiO_3$ film and the heterostructure in (a), showing that the structural distortions in $Nd_{0.93}Pb_{0.07}NiO_3$ are larger than in pure $NdNiO_3$ (the Ni–O–Ni bond angle is thus smaller in doped films). Note that, unlike in Figure 4c,d, here the $NdNiO_3$ film was capped with 5 unit cells of $SrTiO_3$. The vertical dashed line at 0 indicates the interface of the films with the $NdGaO_3$ substrate. The red dashed line at 24 marks the interface between $Nd_{0.93}Pb_{0.07}NiO_3$ and the $SrTiO_3$ capping layer, and the blue dotted line at 33 marks the interface between $NdNiO_3$ and the $SrTiO_3$ capping layer.

of the rare-earth cations (as shown in Figure 5b[51]), with a projected amplitude ΔZ that depends on the tolerance factor, and in turn the Ni–O–Ni bond angle. Due to the trilinear coupling between octahedral tilts and the amplitude of the A-site displacements,[75,76] a smaller Ni–O–Ni bond angle leads to a larger value of ΔZ.[18,19] We take advantage of this coupling and use ΔZ as an indirect relative measurement of the Ni–O–Ni bond angles, rather than directly measuring the oxygen positions from annular bright field images, which may be significantly affected by beam aberrations and sample mistilts.[77]

We have mapped the atomic positions of the A-site cations and have calculated ΔZ for this $x = 0.07$ heterostructure, as well as an undoped $NdNiO_3$ thin film deposited on $NdGaO_3$. Figure 5c is a plot of ΔZ as a function of atomic plane position for these two films. First, we see that the amplitude of the antipolar distortion in the center of each material is different. Figure 5c shows that the amplitude of the antipolar distortion in the pure $NdNiO_3$ film is ≈29 pm, consistent with the ΔZ value of bulk $NdNiO_3$.[51] In contrast, the antipolar distortion in the Pb-doped sample is larger, reaching values of ≈35 pm in the center of the film. Due to the trilinear coupling between the Ni–O–Ni bond angle and the amplitude of the antipolar distortion, ΔZ, we can conclude that the Ni–O–Ni bond angle in the Pb-doped film is smaller than in pure $NdNiO_3$ and the octahedral rotations become more pronounced with Pb doping.

Additionally, we observe that the plot of ΔZ for the pure $NdNiO_3$ film shows an initial dip at the interface with $NdGaO_3$ followed by an increase to a constant value, whereas we do not observe this drop for the Pb-doped film. A similar decrease in the magnitude of the A-site antipolar motions has previously been seen at the interface between $LaFeO_3$ and a $NdGaO_3$ substrate,[18] where the first 4 unit cells of $LaFeO_3$ display a reduced octahedral tilt angle compared to the following layers. This reduction was also shown to occur simultaneously with a local expansion in the out-of-plane lattice parameter,[18] and a similar expansion occurs at the interface for both our films (see Figure S7, Supporting Information). As shown in Figure S7, Supporting Information, the out-of-plane expansion is not correlated with changes in the in-plane lattice parameter, with the latter remaining constant within experimental errors. This effect is most likely associated to the structural mismatch between the layers, but its precise origin is unclear. Nevertheless, despite the behavior at the interface of each film and the substrate, the conclusion of the STEM measurements is clear: the larger amplitude of the antipolar distortion is consistent with a smaller Ni–O–Ni bond angle due to more pronounced octahedral rotations, and therefore a smaller effective ionic radius for the A-site cation in $Nd_{0.93}Pb_{0.07}NiO_3$ compared to $NdNiO_3$. These measurements further validate the conclusion that Pb is in a 4+ valence.

3. Conclusions

We have deposited $Nd_{1-x}Pb_xNiO_3$ thin films with high structural quality and Pb doping levels up to 8%. To maintain the structural quality of the films, as well as a uniform Pb content across their thickness, the $Nd_{1-x}Pb_xNiO_3$ layers need to have Pb content $x \leq 0.08$ and have to be capped with a $SrTiO_3$ layer in situ, immediately after their growth. The T_{MI} of the $Nd_{1-x}Pb_xNiO_3$ films is progressively reduced as a function of increased Pb content; however, it is not completely suppressed for the maximum doping of $x = 0.08$.

Spectroscopic measurements show that a shift from a nominally Ni^{3+} toward a Ni^{2+} valence occurs, providing direct evidence for electron doping. Finally, we find that Pb doping leads to a lower Ni–O–Ni bond angle due to stronger octahedral rotations, and therefore a smaller value of the tolerance factor with respect to pure $NdNiO_3$ films, consistent with a smaller ionic radius for the Pb dopants compared to Nd. Thus, our work demonstrates that, as the Pb content in $Nd_{1-x}Pb_xNiO_3$ thin films is increased, there is a competing effect between charge injection that lowers the transition temperature, and a reduction of the Ni–O–Ni bond angles that increases the transition temperature.

Our results show that A-site substitution with Pb is an appropriate method for electron doping in perovskite rare-earth nickelate systems and provide a systematic study of such doping in epitaxial $NdNiO_3$ films. We believe that these results will contribute to further understanding of the behavior of doped perovskite rare-earth nickelates. Furthermore, they will hopefully inspire future studies to investigate the possibility of inducing electron-doped superconductivity in these systems through topotactic reduction to an infinite-layer phase.

Note: After acceptance of this paper, we have learned of another study on electron-doped $NdNiO_3$ thin films, in which doping with Ce creates an antiferromagnetic metal phase for a specific range of doping, whereas above this doping range the films become completely metallic.[78] We note that such an antiferromagnetic metallic phase has not been observed in our films, and therefore the differences between doping with Ce^{4+} and Pb^{4+} merit further study.

4. Experimental Section

Sample Growth: Multiple $Nd_{1-x}Pb_xNiO_3$ solid solution films were deposited on (110)-oriented orthorhombic $NdGaO_3$ substrates using off-axis radiofrequency magnetron sputtering. The films were deposited by growing sub-monolayer quantities from $Pb_{1.1}NiO_3$ and $NdNiO_3$ ceramic targets and repeating multiple times. A $Pb_{1.1}NiO_3$ target with 10% excess lead was used to compensate for the volatility of Pb. Deposition from the $Pb_{1.1}NiO_3$ target was carried out in a 0.18 Torr atmosphere with an oxygen:argon ratio of 10:35, and RF power of 50 W. The corresponding parameters for $NdNiO_3$ were 0.14 Torr, 10:35, and 50 W. During growth, the temperature of the sample was kept constant at 500 °C, measured by a thermocouple inside the heating block. For reasons discussed in the main text, the studied films were capped with 5 unit cells of $SrTiO_3$ deposited in situ, immediately after the growth of the solid solution, at the same temperature. The growth parameters for $SrTiO_3$ were a pressure of 0.18 Torr, oxygen:argon ratio of 20:28, and RF power of 60 W. Several series of samples were deposited, with compositions varying from $x = 0$ to $x = 0.08$, by fixing the sub-monolayer growth time from the $NdNiO_3$ target and varying the growth time from the $Pb_{1.1}NiO_3$ target.

In cases where solid solutions of two materials were deposited by sequential sub-monolayer deposition from two different sputtering targets, the composition of the resulting film was controlled by the precise calibration of the rates of the constituent materials.[79,80] In the study crystalline films of pure $PbNiO_3$ were not able to be grown to calibrate their growth rate, and therefore a preliminary calibration of the $PbNiO_3$ growth rate was performed by depositing an amorphous film and measuring its thickness with X-ray reflectivity. The $Nd_{1-x}Pb_xNiO_3$

films were then deposited assuming this growth rate was valid for crystalline films as well, and the precise Pb content of each film was determined after deposition using EDX. In the main text, the value measured by EDX was always used when referring to the Pb content x. However, due to the low concentration of Pb in the $x = 0.01$ film, its Pb content was estimated by plotting the measured x versus $Pb_{1.1}NiO_3$ sputtering time for all studied films, and interpolating between $x = 0$ and $x = 0.02$. Finally, it was noted that the A/B cation ratio ((Pb+Nd)/Ni) measured using EDX did not change significantly as a function of Pb doping.

Structural Characterization: Structural characterization of the thin films was performed using an Panalytical X'Pert Pro diffractometer with a Cu Kα source. Atomic force microscopy was used to characterize the surfaces of the thin films, using a Dimension Multimode microscope in tapping mode.

Transport Measurements: Low-temperature resistivity measurements were performed using a probe slowly dipped in liquid helium, as well as an Oxford Instruments Teslatron low-temperature system. For both types of measurements, a Keithley 224 or a Keithley 622X current source were used to supply a current of 100 μA and a voltage was measured using a Keithley 2000 Multimeter or a Keithley 2182A Nanovoltmeter respectively. The measurements were performed in four-point van der Pauw geometry, with the four corners of the sample contacted using Al wire-bonding on sputtered Pt square pads. The resistivity values for the samples were obtained using the van der Pauw formula, with the resistance values for the two orthogonal configurations obtained during separate heating and cooling runs.

X-ray Absorption Spectroscopy: X-ray absorption spectroscopy was used to determine the valence of Ni in the $Nd_{1-x}Pb_xNiO_3$ thin films. The measurements were performed at the EPFL/PSI X-Treme beamline at the Swiss Light Source, Paul Scherrer Institut, Villigen, Switzerland.[81] The measurements were carried out in total electron yield mode at room temperature. The X-ray absorption spectra were the average of linear horizontal and vertical polarization taken in normal incidence.

Scanning Transmission Electron Microscopy: Scanning transmission electron microscopy measurements were used to obtain information on the local structure of the films, using a double aberration-corrected FEI (Thermo Fisher Scientific) Titan Themis 60-300 electron microscope equipped with a double aberration-corrector (CEOS) and a high brightness field emission gun with a monochromator. High quality high-angle annular dark-field (HAADF) images were acquired using a convergence semi-angle of 20 mrad, a 300 kV high tension, and low beam currents (30–40 pA) to prevent electron beam damage and contamination. To correct the linear and non-linear scanning distortions, a series of 24 iterative 90° rotated HAADF frames were acquired from each analyzed area, and afterward aligned using the SmartAlign plug-in for DigitalMicrograph.[82] The coordinates associated to the central position of each Pb/Nd column were estimated using a 2D Gaussian fitting procedure using the Atomap script.[83]

Energy-Dispersive X-ray Spectroscopy: EDX maps were acquired on the same microscope, using a four quadrant Super-X windowless silicon drift detector system and beam currents of ≈100–250 pA. The maps were recorded and analyzed using Thermo Fisher Scientific Velox software. The Pb and Nd content was estimated by integrating the EDX signal from a central region of the analyzed films and then quantifying the Pb L and Nd L peaks of the spectrum using the Cliff–Lorimer approach with Brown–Powell ionization cross-section models.

Electron Energy-Loss Spectroscopy: EELS spectrum images were similarly acquired on the same microscope, but using a high tension of 200 kV. The data were recorded with a Gatan GIF Quantum ERS spectrometer, using a convergence semi-angle of ≈17 mrad, a collection angle of ≈47 mrad, 0.1 s dwell time and 0.1 eV per channel dispersion. The zero-loss peak was acquired simultaneously to the core-loss region using a dual-EELS configuration. The zero-loss peak was used to align all the spectra belonging to the same spectrum image. The beam was slightly monochromated to improve the energy resolution while keeping a beam current of ≈80 pA, reaching a zero-loss peak full-width at half maximum of ≈0.4 eV. More acquisition details can be found in a previous publication.[84] The two TEM lamellae used for the fine-structure analysis, prepared with the focused ion beam, were transferred to the same Cu grid so that all EELS spectra were acquired in the same session without changing the acquisition conditions.

Supporting Information

Supporting Information is available from the Wiley Online Library or from the author.

Acknowledgements

The authors gratefully acknowledge Marco Lopes for technical support, Jennifer Fowlie and Stefano Gariglio for useful discussions during the initial stages of this work. This work was supported by the Swiss National Science Foundation through Division II grant nos. 200020_179155 (M.H., B.M., C.D., and J.-M.T.), PP00P2_170564 (M.G., G.D.L., J.S., and S.J.), the National Centers of Competence in Research MARVEL scheme under grant no. 51NF40-182892 (M.G. and S.J.), and the European Research Council under the European Union's Seventh Framework Programme (FP7/2007-2013)/ERC grant agreement no. 319286 (Q-MAC) (M.H., B.M., C.D., and J.-M.T.). The authors acknowledge the Paul Scherrer Institute and the X-Treme (X07MA) beamline staff for support during the X-ray absorption spectroscopy experiment, and the CIME at EPFL for access to electron microscopy facilities.

Conflict of Interest

The authors declare no conflict of interest.

Data Availability Statement

The data that support the findings of this study are openly available in the Yareta repository at https://doi.org/10/grrhhn.

Keywords

doping, metal–insulator transitions, $NdNiO_3$, octahedral rotations, $PbNiO_3$, rare-earth nickelates, X-ray absorption spectroscopy

Received: October 27, 2022
Revised: January 27, 2023
Published online: March 16, 2023

[1] M. Imada, A. Fujimori, Y. Tokura, *Rev. Mod. Phys.* **1998**, *70*, 1039.
[2] Y. Tokura, *Rep. Prog. Phys.* **2006**, *69*, 797.
[3] B. Keimer, S. A. Kivelson, M. R. Norman, S. Uchida, J. Zaanen, *Nature* **2015**, *518*, 179.
[4] M. L. Medarde, *J. Phys. Condens. Matter* **1997**, *9*, 1679.
[5] G. Catalan, *Phase Transitions* **2008**, *81*, 729.
[6] S. Catalano, M. Gibert, J. Fowlie, J. Íñiguez, J.-M. Triscone, J. Kreisel, *Rep. Prog. Phys.* **2018**, *81*, 046501.
[7] G. Catalan, R. M. Bowman, J. M. Gregg, *Phys. Rev. B* **2000**, *62*, 7892.
[8] J. Son, P. Moetakef, J. M. LeBeau, D. Ouellette, L. Balents, S. J. Allen, S. Stemmer, *Appl. Phys. Lett.* **2010**, *96*, 062114.
[9] R. Scherwitzl, P. Zubko, I. G. Lezama, S. Ono, A. F. Morpurgo, G. Catalan, J. M. Triscone, *Adv. Mater.* **2010**, *22*, 5517.

[10] P. H. Xiang, N. Zhong, C. G. Duan, X. D. Tang, Z. G. Hu, P. X. Yang, Z. Q. Zhu, J. H. Chu, *J. Appl. Phys.* **2013**, *114*, 243713.
[11] X. K. Lian, F. Chen, X. L. Tan, P. F. Chen, L. F. Wang, G. Y. Gao, S. W. Jin, W. B. Wu, *Appl. Phys. Lett.* **2013**, *103*, 172110.
[12] S. Catalano, M. Gibert, V. Bisogni, O. E. Peil, F. He, R. Sutarto, M. Viret, P. Zubko, R. Scherwitzl, A. Georges, G. A. Sawatzky, T. Schmitt, J.-M. Triscone, *APL Mater.* **2014**, *2*, 116110.
[13] E. Benckiser, M. W. Haverkort, S. Brück, E. Goering, S. Macke, A. Frañó, X. Yang, O. K. Andersen, G. Cristiani, H. U. Habermeier, A. V. Boris, I. Zegkinoglou, P. Wochner, H. J. Kim, V. Hinkov, B. Keimer, *Nat. Mater.* **2011**, *10*, 189.
[14] M. Gibert, P. Zubko, R. Scherwitzl, J. Íñiguez, J.-M. Triscone, *Nat. Mater.* **2012**, *11*, 195.
[15] M. Gibert, M. Viret, A. Torres-Pardo, C. Piamonteze, P. Zubko, N. Jaouen, J.-M. Tonnerre, A. Mougin, J. Fowlie, S. Catalano, A. Gloter, O. Stéphan, J.-M. Triscone, *Nano Lett.* **2015**, *15*, 7355.
[16] A. S. Disa, D. P. Kumah, A. Malashevich, H. Chen, D. A. Arena, E. D. Specht, S. Ismail-Beigi, F. J. Walker, C. H. Ahn, *Phys. Rev. Lett.* **2015**, *114*, 026801.
[17] M. Gibert, M. Viret, P. Zubko, N. Jaouen, J.-M. Tonnerre, A. Torres-Pardo, S. Catalano, A. Gloter, O. Stéphan, J.-M. Triscone, *Nat. Commun.* **2016**, *7*, 11227.
[18] Z. Liao, N. Gauquelin, R. J. Green, K. Müller-Caspary, I. Lobato, L. Li, S. Van Aert, J. Verbeeck, M. Huijben, M. N. Grisolia, V. Rouco, R. El Hage, J. E. Villegas, A. Mercy, M. Bibes, P. Ghosez, G. A. Sawatzky, G. Rijnders, G. Koster, *Proc. Natl. Acad. Sci. U. S. A.* **2018**, *115*, 9515.
[19] C. Domínguez, A. B. Georgescu, B. Mundet, Y. Zhang, J. Fowlie, A. Mercy, A. Waelchli, S. Catalano, D. T. L. Alexander, P. Ghosez, A. Georges, A. J. Millis, M. Gibert, J.-M. Triscone, *Nat. Mater.* **2020**, *19*, 1182.
[20] R. Scherwitzl, P. Zubko, C. Lichtensteiger, J.-M. Triscone, *Appl. Phys. Lett.* **2009**, *95*, 222114.
[21] J. Son, B. Jalan, A. P. Kajdos, L. Balents, S. James Allen, S. Stemmer, *Appl. Phys. Lett.* **2011**, *99*, 192107.
[22] R. Scherwitzl, S. Gariglio, M. Gabay, P. Zubko, M. Gibert, J.-M. Triscone, *Phys. Rev. Lett.* **2011**, *106*, 246403.
[23] J. Fowlie, M. Gibert, G. Tieri, A. Gloter, J. Íñiguez, A. Filippetti, S. Catalano, S. Gariglio, A. Schober, M. Guennou, J. Kreisel, O. Stéphan, J.-M. Triscone, *Adv. Mater.* **2017**, *29*, 1605197.
[24] M. Hepting, R. J. Green, Z. Zhong, M. Bluschke, Y. E. Suyolcu, S. Macke, A. Frano, S. Catalano, M. Gibert, R. Sutarto, F. He, G. Cristiani, G. Logvenov, Y. Wang, P. A. van Aken, P. Hansmann, M. Le Tacon, J. M. Triscone, G. A. Sawatzky, B. Keimer, E. Benckiser, *Nat. Phys.* **2018**, *14*, 1097.
[25] A. D. Caviglia, M. Först, R. Scherwitzl, V. Khanna, H. Bromberger, R. Mankowsky, R. Singla, Y.-D. Chuang, W. S. Lee, O. Krupin, W. F. Schlotter, J. J. Turner, G. L. Dakovski, M. P. Minitti, J. Robinson, V. Scagnoli, S. B. Wilkins, S. A. Cavill, M. Gibert, S. Gariglio, P. Zubko, J.-M. Triscone, J. P. Hill, S. S. Dhesi, A. Cavalleri, *Phys. Rev. B* **2013**, *88*, 220401.
[26] M. Först, A. D. Caviglia, R. Scherwitzl, R. Mankowsky, P. Zubko, V. Khanna, H. Bromberger, S. B. Wilkins, Y. D. Chuang, W. S. Lee, W. F. Schlotter, J. J. Turner, G. L. Dakovski, M. P. Minitti, J. Robinson, S. R. Clark, D. Jaksch, J. M. Triscone, J. P. Hill, S. S. Dhesi, A. Cavalleri, *Nat. Mater.* **2015**, *14*, 883.
[27] G. Mattoni, N. Manca, M. Hadjimichael, P. Zubko, A. J. H. van der Torren, C. Yin, S. Catalano, M. Gibert, F. Maccherozzi, Y. Liu, S. S. Dhesi, A. D. Caviglia, *Phys. Rev. Mater.* **2018**, *2*, 085002.
[28] D. Li, K. Lee, B. Y. Wang, M. Osada, S. Crossley, H. R. Lee, Y. Cui, Y. Hikita, H. Y. Hwang, *Nature* **2019**, *572*, 624.
[29] S. Zeng, C. S. Tang, X. Yin, C. Li, M. Li, Z. Huang, J. Hu, W. Liu, G. J. Omar, H. Jani, Z. S. Lim, K. Han, D. Wan, P. Yang, S. J. Pennycook, A. T. Wee, A. Ariando, *Phys. Rev. Lett.* **2020**, *125*, 147003.
[30] M. Osada, B. Y. Wang, B. H. Goodge, K. Lee, H. Yoon, K. Sakuma, D. Li, M. Miura, L. F. Kourkoutis, H. Y. Hwang, *Nano Lett.* **2020**, *20*, 5735.
[31] M. Osada, B. Y. Wang, K. Lee, D. Li, H. Y. Hwang, *Phys. Rev. Mater.* **2020**, *4*, 121801.
[32] D. Li, B. Y. Wang, K. Lee, S. P. Harvey, M. Osada, B. H. Goodge, L. F. Kourkoutis, H. Y. Hwang, *Phys. Rev. Lett.* **2020**, *125*, 027001.
[33] M. Osada, B. Y. Wang, B. H. Goodge, S. P. Harvey, K. Lee, D. Li, L. F. Kourkoutis, H. Y. Hwang, *Adv. Mater.* **2021**, *33*, 2104083.
[34] G. A. Pan, D. Ferenc Segedin, H. LaBollita, Q. Song, E. M. Nica, B. H. Goodge, A. T. Pierce, S. Doyle, S. Novakov, D. Córdova Carrizales, A. T. N'Diaye, P. Shafer, H. Paik, J. T. Heron, J. A. Mason, A. Yacoby, L. F. Kourkoutis, O. Erten, C. M. Brooks, A. S. Botana, J. A. Mundy, *Nat. Mater.* **2022**, *21*, 160.
[35] B.-X. Wang, H. Zheng, E. Krivyakina, O. Chmaissem, P. P. Lopes, J. W. Lynn, L. C. Gallington, Y. Ren, S. Rosenkranz, J. F. Mitchell, D. Phelan, *Phys. Rev. Mater.* **2020**, *4*, 084409.
[36] P. Puphal, Y.-M. Wu, K. Fürsich, H. Lee, M. Pakdaman, J. A. N. Bruin, J. Nuss, Y. E. Suyolcu, P. A. van Aken, B. Keimer, M. Isobe, M. Hepting, *Sci. Adv.* **2021**, *7*, eabl8091.
[37] Y. Dong, H. Xu, Z. Luo, H. Zhou, D. D. Fong, W. Wu, C. Gao, *APL Mater.* **2017**, *5*, 051101.
[38] I. V. Nikulin, M. A. Novojilov, A. R. Kaul, S. N. Mudretsova, S. V. Kondrashov, *Mater. Res. Bull.* **2004**, *39*, 775.
[39] J. Shi, Y. Zhou, S. Ramanathan, *Nat. Commun.* **2014**, *5*, 4860.
[40] Y. Zhou, X. Guan, H. Zhou, K. Ramadoss, S. Adam, H. Liu, S. Lee, J. Shi, M. Tsuchiya, D. D. Fong, S. Ramanathan, *Nature* **2016**, *534*, 231.
[41] S. Heo, C. Oh, J. Son, H. M. Jang, *Sci. Rep.* **2017**, *7*, 4681.
[42] Q. Guo, S. Farokhipoor, C. Magén, F. Rivadulla, B. Noheda, *Nat. Commun.* **2020**, *11*, 2949.
[43] Q. Guo, B. Noheda, *npj Quantum Mater.* **2021**, *6*, 72.
[44] S.-W. Cheong, H. Hwang, B. Batlogg, A. Cooper, P. Canfield, *Phys. B Condens. Matter* **1994**, *194–196*, 1087.
[45] J. García-Muñoz, M. Suaaidi, J. Alonso, M. Martínez-Lope, *Phys. C Supercond.* **1994**, *235–240*, 1475.
[46] J. Alonso, M. Martínez-Lope, M. Hidalgo, *J. Solid State Chem.* **1995**, *116*, 146.
[47] J. L. García-Muñoz, M. Suaaidi, M. J. Martínez-Lope, J. A. Alonso, *Phys. Rev. B* **1995**, *52*, 13563.
[48] R. D. Shannon, *Acta Crystallogr. Sect. A* **1976**, *32*, 751.
[49] P.-H. Xiang, S. Asanuma, H. Yamada, I. H. Inoue, H. Akoh, A. Sawa, *Appl. Phys. Lett.* **2010**, *97*, 032114.
[50] L. Wang, L. Chang, X. Yin, A. Rusydi, L. You, Y. Zhou, L. Fang, J. Wang, *J. Phys. Condens. Matter* **2017**, *29*, 025002.
[51] J. L. García-Muñoz, J. Rodríguez-Carvajal, P. Lacorre, J. B. Torrance, *Phys. Rev. B* **1992**, *46*, 4414.
[52] J. Torrance, P. Lacorre, A. Nazzal, E. Ansaldo, C. Niedermayer, *Phys. Rev. B* **1992**, *45*, 8209.
[53] J. L. García-Muñoz, J. Rodríguez-Carvajal, P. Lacorre, *Europhys. Lett.* **1992**, *20*, 241.
[54] J. L. García-Muñoz, J. Rodríguez-Carvajal, P. Lacorre, *Phys. Rev. B* **1994**, *50*, 978.
[55] Y. Inaguma, K. Tanaka, T. Tsuchiya, D. Mori, T. Katsumata, T. Ohba, K. I. Hiraki, T. Takahashi, H. Saitoh, *J. Am. Chem. Soc.* **2011**, *133*, 16920.
[56] J. B. Goodenough, J. Zhou, *Sci. Technol. Adv. Mater.* **2015**, *16*, 036003.
[57] C. L. Yaws, *Handbook of Vapor Pressure Volume 4: Inorganic Compounds and Elements*, Gulf Publishing Company, Houston, TX **1995**.
[58] R. H. Lamoreaux, D. L. Hildenbrand, L. Brewer, *J. Phys. Chem. Ref. Data* **1987**, *16*, 419.
[59] C. Lichtensteiger, *J. Appl. Crystallogr.* **2018**, *51*, 1745.
[60] L. Wang, S. Dash, L. Chang, L. You, Y. Feng, X. He, K. J. Jin, Y. Zhou, H. G. Ong, P. Ren, S. Wang, L. Chen, J. Wang, *ACS Appl. Mater. Interfaces* **2016**, *8*, 9769.

[61] T. Onozuka, A. Chikamatsu, T. Katayama, Y. Hirose, I. Harayama, D. Sekiba, E. Ikenaga, M. Minohara, H. Kumigashira, T. Hasegawa, *ACS Appl. Mater. Interfaces* **2017**, *9*, 10882.
[62] Y. Sun, M. Kotiuga, D. Lim, B. Narayanan, M. Cherukara, Z. Zhang, Y. Dong, R. Kou, C.-J. Sun, Q. Lu, I. Waluyo, A. Hunt, H. Tanaka, A. N. Hattori, S. Gamage, Y. Abate, V. G. Pol, H. Zhou, S. K. R. S. Sankaranarayanan, B. Yildiz, K. M. Rabe, S. Ramanathan, *Proc. Natl. Acad. Sci. U. S. A.* **2018**, *115*, 9672.
[63] M. Kotiuga, Z. Zhang, J. Li, F. Rodolakis, H. Zhou, R. Sutarto, F. He, Q. Wang, Y. Sun, Y. Wang, N. A. Aghamiri, S. B. Hancock, L. P. Rokhinson, D. P. Landau, Y. Abate, J. W. Freeland, R. Comin, S. Ramanathan, K. M. Rabe, *Proc. Natl. Acad. Sci. U. S. A.* **2019**, *116*, 21992.
[64] P. Lacorre, J. Torrance, J. Pannetier, A. Nazzal, P. Wang, T. Huang, *J. Solid State Chem.* **1991**, *91*, 225.
[65] X. Granados, J. Fontcuberta, X. Obradors, L. Mañosa, J. B. Torrance, *Phys. Rev. B* **1993**, *48*, 11666.
[66] A. J. Hauser, E. Mikheev, N. E. Moreno, J. Hwang, J. Y. Zhang, S. Stemmer, *Appl. Phys. Lett.* **2015**, *106*, 092104.
[67] G. van der Laan, J. Zaanen, G. A. Sawatzky, R. Karnatak, J.-M. Esteva, *Phys. Rev. B* **1986**, *33*, 4253.
[68] T. Mizokawa, A. Fujimori, T. Arima, Y. Tokura, N. Mōri, J. Akimitsu, *Phys. Rev. B* **1995**, *52*, 13865.
[69] C. Piamonteze, F. M. F. de Groot, H. C. N. Tolentino, A. Y. Ramos, N. E. Massa, J. A. Alonso, M. J. Martínez-Lope, *Phys. Rev. B* **2005**, *71*, 020406.
[70] J. W. Freeland, M. Van Veenendaal, J. Chakhalian, *J. Electron Spectros. Relat. Phenom.* **2016**, *208*, 56.
[71] V. Bisogni, S. Catalano, R. J. Green, M. Gibert, R. Scherwitzl, Y. Huang, V. N. Strocov, P. Zubko, S. Balandeh, J.-M. Triscone, G. Sawatzky, T. Schmitt, *Nat. Commun.* **2016**, *7*, 13017.
[72] J. Chen, H. Hu, J. Wang, T. Yajima, B. Ge, X. Ke, H. Dong, Y. Jiang, N. Chen, *Mater. Horiz.* **2019**, *6*, 788.
[73] T. H. Kim, T. R. Paudel, R. J. Green, K. Song, H.-S. Lee, S.-Y. Choi, J. Irwin, B. Noesges, L. J. Brillson, M. S. Rzchowski, G. A. Sawatzky, E. Y. Tsymbal, C. B. Eom, *Phys. Rev. B* **2020**, *101*, 121105.
[74] Z. Zhang, D. Schwanz, B. Narayanan, M. Kotiuga, J. A. Dura, M. Cherukara, H. Zhou, J. W. Freeland, J. Li, R. Sutarto, F. He, C. Wu, J. Zhu, Y. Sun, K. Ramadoss, S. S. Nonnenmann, N. Yu, R. Comin, K. M. Rabe, S. K. Sankaranarayanan, S. Ramanathan, *Nature* **2018**, *553*, 68.
[75] S. Amisi, E. Bousquet, K. Katcho, P. Ghosez, *Phys. Rev. B* **2012**, *85*, 064112.
[76] N. Miao, N. C. Bristowe, B. Xu, M. J. Verstraete, P. Ghosez, *J. Phys. Condens. Matter* **2014**, *26*, 035401.
[77] D. Zhou, K. Müller-Caspary, W. Sigle, F. F. Krause, A. Rosenauer, P. A. van Aken, *Ultramicroscopy* **2016**, *160*, 110.
[78] Q. Song, S. Doyle, G. A. Pan, I. El Baggari, D. Ferenc Segedin, D. Còrdova Carrizales, J. Nordlander, C. Tzschaschel, J. R. Ehrets, Z. Hasan, H. El-Sherif, J. Krishna, C. Hanson, H. LaBollita, A. Bostwick, C. Jozwiak, E. Rotenberg, S.-Y. Xu, A. Lanzara, A. T. N'Diaye, C. A. Heikes, Y. Liu, H. Paik, C. M. Brooks, B. Pamuk, J. T. Heron, P. Shafer, W. D. Ratcliff, A. S. Botana, L. Moreschini, J. A. Mundy, *Nat. Phys.* **2023**, 10, https://doi.org/10.1038/s41567-022-01907-2.
[79] S. Fernandez-Peña, C. Lichtensteiger, P. Zubko, C. Weymann, S. Gariglio, J.-M. Triscone, *APL Mater.* **2016**, *4*, 086105.
[80] J. Fowlie, B. Mundet, C. Toulouse, A. Schober, M. Guennou, C. Domínguez, M. Gibert, D. T. L. Alexander, J. Kreisel, J. M. Triscone, *APL Mater.* **2021**, *9*, 081119.
[81] C. Piamonteze, U. Flechsig, S. Rusponi, J. Dreiser, J. Heidler, M. Schmidt, R. Wetter, M. Calvi, T. Schmidt, H. Pruchova, J. Krempasky, C. Quitmann, H. Brune, F. Nolting, *J. Synchrotron Radiat.* **2012**, *19*, 661.
[82] L. Jones, H. Yang, T. J. Pennycook, M. S. J. Marshall, S. Van Aert, N. D. Browning, M. R. Castell, P. D. Nellist, *Adv. Struct. Chem. Imaging* **2015**, *1*, 8.
[83] M. Nord, P. E. Vullum, I. MacLaren, T. Tybell, R. Holmestad, *Adv. Struct. Chem. Imaging* **2017**, *3*, 9.
[84] B. Mundet, C. Domínguez, J. Fowlie, M. Gibert, J.-M. Triscone, D. T. L. Alexander, *Nano Lett.* **2021**, *21*, 2436.